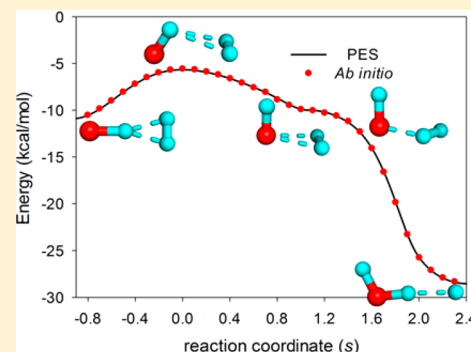


A Full-Dimensional Global Potential Energy Surface of $\text{H}_3\text{O}^+(\tilde{a}^3\text{A})$ for the $\text{OH}^+(\tilde{\text{X}}^3\Sigma^-) + \text{H}_2(\tilde{\text{X}}^1\Sigma_g^+) \rightarrow \text{H}^2\text{S} + \text{H}_2\text{O}^+(\tilde{\text{X}}^2\text{B}_1)$ Reaction

Anyang Li and Hua Guo*

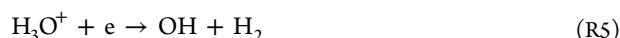
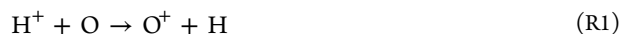
Department of Chemistry and Chemical Biology, University of New Mexico, Albuquerque, New Mexico 87131, United States

ABSTRACT: An accurate full-dimensional global potential energy surface (PES) is developed for the title reaction. The PES was based on $\sim 30\,000$ points at the Davidson corrected multireference configuration interaction level with the aug-cc-pVQZ basis set (MRCI+Q/AVQZ). The ab initio points were fitted using the permutation invariant polynomial-neural network (PIP-NN) method with a root-mean-square error of about 3.0 meV or 24 cm^{-1} . The kinetics of the $\text{OH}^+ + \text{H}_2$ and $\text{OH}^+ + \text{D}_2$ reactions were investigated on the PIP-NN PES using a quasi-classical trajectory method and the calculated thermal rate coefficients are in good agreement with the available experimental data. Furthermore, it is predicted based on the PES using the Sudden Vector Projection model that the rotational excitation of OH^+ enhances the reaction at low collision energies.



I. INTRODUCTION

The H_xO^+ ($x = 1, 2, 3$) molecular ions are important species in interstellar oxygen chemistry.^{1–3} These ions have recently been found in several regions of the outer space by the Herschel space observatory.^{4–6} The hydroxyl radical and water molecule are thought to form in interstellar media through the following reactions



The three ion–molecule reactions R2, R3, and R4 are the most important steps in this process, and their rate coefficients have been extensively measured.^{7–20} In addition, the reaction dynamics of reactions R2 and R4 have been investigated by Ng and co-workers,^{20–24} who found that the reactivity of reaction R4 is strongly enhanced by H_2O^+ rotational excitations. The rotational enhancement was surprising as mode specificity is typically absent for barrierless complex-forming reactions.²⁵

Several theoretical studies of the R2 reaction dynamics^{26–29} have been reported based on an accurate potential energy surface (PES) for the lowest quadruplet state of $\text{H}_2\text{O}^+(\tilde{a}^4\text{A}'')$.³⁰ More recently, we systematically investigated the kinetics and dynamics of the R4 reaction on a full-dimensional global PES of $\text{H}_4\text{O}^+(\text{X}^2\text{A})$.^{24,31} In particular, the observed rotational enhancement of reactivity was explained by the coupling of a H_2O^+

rotational degree of freedom with the reaction coordinate at a submerged saddle point along the reaction path.³¹ However, the R3 reaction has never been investigated theoretically, although the hydronium ion (H_3O^+) has attracted much recent theoretical attention as it is the simplest molecular ion to undergo large-amplitude inversion tunneling.^{32–36} It should, however, be noted that these studies were concerned with the ground electronic state of $\text{H}_3\text{O}^+(\tilde{\text{X}}^1\text{A})$, which correlates with the electronically excited hydroxyl ion and ground-state hydrogen molecule ($\text{OH}^+(\tilde{a}^1\Delta) + \text{H}_2(\tilde{\text{X}}^1\Sigma_g^+)$). In this work, we focus on the R3 reaction between the hydroxyl ion and hydrogen molecule in their ground electronic states ($\text{OH}^+(\tilde{\text{X}}^3\Sigma^-) + \text{H}_2(\tilde{\text{X}}^1\Sigma_g^+)$), which leads to the formation of H_3O^+ in its lowest triplet state $\text{H}_3\text{O}^+(\tilde{a}^3\text{A})$. Figure 1 presents the schematic energy diagram for the $\text{OH}^+ + \text{H}_2 \rightarrow \text{H}_2\text{O}^+ + \text{H}$ reaction on two lowest-lying electronic states of H_3O^+ . As it

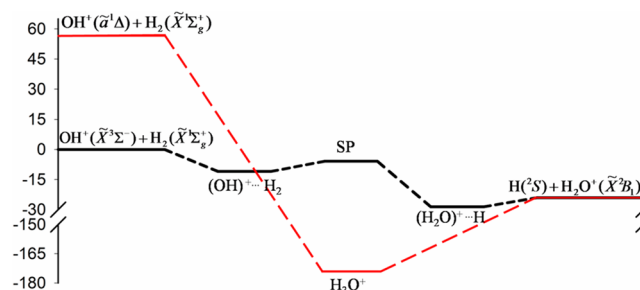


Figure 1. Schematic energy diagram for the $\text{OH}^+ + \text{H}_2 \rightarrow \text{H}_2\text{O}^+ + \text{H}$ reaction on two lowest-lying electronic states of H_3O^+ (black for the $\tilde{a}^3\text{A}$ state and red for the $\tilde{\text{X}}^1\text{A}$ state).

Received: October 4, 2014

Revised: October 23, 2014

Published: October 24, 2014

shows, the $\text{H}_3\text{O}^+(\tilde{X}^1\text{A})$ minimum is quite stable (~ 150 kcal/mol below the product asymptote of the $\text{OH}^+(\tilde{a}^1\Delta) + \text{H}_2(\tilde{X}^1\Sigma_g^+) \rightarrow \text{H}(\tilde{2}\text{S}) + \text{H}_2\text{O}^+(\tilde{X}^2\text{B}_1)$ reaction).

Also shown in Figure 1, the $\text{OH}^+(\tilde{X}^3\Sigma^-) + \text{H}_2(\tilde{X}^1\Sigma_g^+) \rightarrow \text{H}(\tilde{2}\text{S}) + \text{H}_2\text{O}^+(\tilde{X}^2\text{B}_1)$ reaction is barrierless and exoergic. However, the reaction pathway includes a submerged saddle point, which is very similar to the R4 reaction.³¹ As a first approximation, the intersystem crossing between the singlet and triplet PESs is assumed to be inefficient for this system. As a result, the title reaction can be treated adiabatically on the triplet PES. Given its small numbers of electrons (10) and internal coordinates (6), it could serve as an ideal prototype for quantum mechanical studies of ion–molecule reaction dynamics in polyatomic systems. To facilitate such studies, we report in this work the first full-dimensional global PES for the lowest triplet state of H_3O^+ designed for the accurate characterization of the title reaction R3. The PES was constructed from more than 30 000 ab initio points at the multireference configuration interaction level with a large correlation-consistent basis set. The kinetics were then investigated using a quasi-classical trajectory (QCT) method. The good agreement with available experimental rate coefficients provides strong evidence for the accuracy of the PES. We further predict based on PES using the recently proposed Sudden Vector Projection model^{37,38} that the rotation of OH^+ enhances reactivity. The remainder of this paper is organized as follows. Section II outlines the details of the ab initio calculations, PES fitting, and QCT calculations. The results and discussion are presented in section III, and the conclusion is given in section IV.

II. THEORY

A. Ab Initio Calculations. To assess the performance of various ab initio methods, the geometries of the reactant, product, and all the stationary points along the reaction pathway were first determined. The methods used include a spin-restricted open-shell density functional theory (RO-DFT) with the MPW1K functional,³⁹ an explicitly correlated unrestricted coupled cluster singles, doubles, and perturbative triples (UCCSD(T)-F12a) method,^{40–42} and an internally contracted multireference configuration interaction method with the Davidson correction (icMRCI+Q).^{43–45} The augmented correlation-consistent polarized valence quadruple- ζ (aug-cc-pVQZ or AVQZ) basis set⁴⁶ was employed in both MPW1K and MRCI calculations, and the correlation-consistent basis set for molecular core–valence effects with explicitly correlated wave functions⁴¹ (cc-pCVTZ-F12) was used in the UCCSD(T) calculations. The MRCI calculations were carried out using the dynamically weighted^{47,48} state-averaged complete active space self-consistent field^{49,50} (DW-SA-CASSCF) orbitals with all the CAS configurations as the reference configuration state functions. The DW-SA-CASSCF calculations with three lowest triplet states were carried out with the full valence active space (8e, 7o), while the 1s orbital of the oxygen atom was kept doubly occupied but fully optimized. In the generalized DW scheme, the energy dependence is weighted as⁴⁸ $\text{sech}^2(\Delta) = [2/(\exp(-\beta\Delta) + \exp(\beta\Delta))]^2$, with Δ being the energy from the lowest triplet state and $\beta^{-1} = 3.0$ eV. All ab initio calculations were performed with MOLPRO,⁵¹ except the MPW1K ones, which employed Gaussian 09.⁵²

B. Potential Energy Surface. Similar to our previous work on the $\text{H}_2\text{O}^+ + \text{H}_2$ system R4,³¹ the fitted PES for the title

reaction R3 consists of two regions. The first characterizes long-range interactions between the OH^+ ion and H_2 molecule, which are dominated by the charge–induced dipole and charge–quadrupole interactions. The second, which is based on ab initio calculations, describes all other regions. These two segments are connected using a switching function, as discussed below.

The long-range part of the PES, denoted as V_{LR} , has the following form:

$$V_{\text{LR}} = V_{\text{OH}^+ + \text{H}_2} + V_{\text{ES}} \quad (1)$$

Here, $V_{\text{OH}^+ + \text{H}_2}$ represents the sum of the isolated OH^+ and H_2 potential energy curves, which were spline-interpolated from ab initio data points with an $\text{OH}^+ - \text{H}_2$ separation of 100.0 Å, and the electrostatic term V_{ES} includes the dominant charge–quadrupole $V_{q\Theta}(\vec{R}_c, \vartheta)$ and charge–induced dipole $V_{qa}(\vec{R}_c, \vartheta)$ interactions:⁵³

$$\begin{aligned} V_{\text{ES}}(\vec{R}_c, \vartheta) &= V_{q\Theta}(\vec{R}_c, \vartheta) + V_{qa}(\vec{R}_c, \vartheta) \\ &= \frac{q\Theta(3\cos^2\vartheta - 1)}{2\vec{R}_c^3} - \frac{q^2\left[\alpha + \frac{\alpha_{\parallel} - \alpha_{\perp}}{3}(3\cos^2\vartheta - 1)\right]}{2\vec{R}_c^4} \end{aligned} \quad (2)$$

where q denotes the charge of the molecular ion (+1). The quadrupole moment of H_2 is $\Theta = 0.63$ esu, its parallel and perpendicular components of the polarizability are $\alpha_{\parallel} = 0.4793$ Å³ and $\alpha_{\perp} = 0.1653$ Å³, and its polarizability is $\alpha = \alpha_{\parallel} + 2\alpha_{\perp} = 0.81$ Å³.⁵⁴ \vec{R}_c is the separation between the center of charge of the OH^+ ion and the center of mass of hydrogen molecule, and ϑ is the angle between \vec{R}_c and the H–H internuclear bond vector. The center of charge is defined as $\vec{r}_{\text{OH}^+} = (\sum_i q_i \vec{r}_i) / (\sum_i q_i)$ by analogy to the center of mass, where \vec{r}_i are the atomic coordinates and the atomic charges q_i were calculated using the charges from the electrostatic potential on a grid (CHelpG) point selection algorithm.⁵⁵ The analytical representation of the long-range interactions is advantageous.⁵⁶ First, it reduces the amount of ab initio calculations when the two reactants are separated by large distances, where ab initio calculations may be difficult. Second, it avoids fitting errors, which can be significant compared with the magnitude of the potential energy in this region.

The second part of the PES, denoted as V_{fit} , was fit to ab initio points using the permutation invariant polynomial neural network (PIP-NN) approach.^{57,58} As discussed below, all ab initio calculations were carried out at the level of MRCI+Q/AVQZ because of the multireference character of the system. In order to provide an accurate global PES with reasonable computational costs, the following strategy was employed to sample the ab initio points. First, stationary points along the reaction pathway were surveyed to determine the ranges of configurations and energies necessary for the PES. Points with energies higher than 120 kcal/mol relative to the reactant asymptote ($\text{OH}^+ + \text{H}_2$) were discarded. Second, grids of points in the appropriate coordinates were used in various regions to sample relevant configurations. To further explore the topography of the PES, batches of trajectories at various energies were dispatched to search for unphysical regions of the PES resulted from the lack of ab initio data points. These geometries were screened to remove points that are too close to the existing ones. The closeness between a new point $\{\vec{d}_i\}$ and one

Table 1. Geometries in Internal Coordinates (Distances in Å and Angles in deg) of the Stationary Points for the $\text{OH}^+ + \text{H}_2 \rightarrow \text{H}_2\text{O}^+ + \text{H}$ Reaction^a

species	method	r_{H1H2} (Å)	r_{OH2} (Å)	r_{OH3} (Å)	θ_{H1OH3} (deg)	θ_{H2OH3} (deg)	ϕ_{H1H2OH3} (deg)
OH ⁺ + H ₂	CASSCF	0.7486		1.0284			
	MPW1K	0.7428		1.0287			
	UCCSD(T)	0.7416		1.0287			
	MRCI	0.7420		1.0280			
	PES	0.7419		1.0287			
	expt	0.7414 ^b		1.0289 ^c			
(OH) ⁺ ...H ₂	CASSCF	0.7500	2.4699	1.0974	8.95	8.95	0.00
	MPW1K	0.7635	2.4566	1.0962	8.94	8.94	0.00
	UCCSD(T)	0.7637	2.4436	1.1052	8.92	8.92	0.00
	MRCI	0.7618	2.4510	1.1008	8.94	8.94	0.00
	PES	0.7629	2.4552	1.1024	8.94	8.94	0.00
SP	CASSCF	0.7600	2.3897	1.0221	53.90	53.90	84.05
	MPW1K	0.7569	2.4043	1.0273	56.54	56.54	83.98
	MRCI	0.7552	2.4010	1.0271	52.36	52.36	83.10
	PES	0.7562	2.3904	1.0279	52.53	52.53	82.95
(H ₂ O) ⁺ ...H	CASSCF	1.5555	1.0352	0.9970	112.56	108.46	179.88
	MPW1K	1.5367	1.0274	0.9978	111.24	109.37	179.64
	UCCSD(T)	1.5240	1.0288	0.9973	111.47	109.44	179.98
	MRCI	1.5275	1.0292	0.9980	111.21	109.32	179.89
	PES	1.5258	1.0304	0.9984	111.07	109.22	180.00
H ₂ O ⁺ + H	CASSCF		1.0041	1.0041		107.86	
	MPW1K		1.0009	1.0009		109.41	
	UCCSD(T)		1.0006	1.0006		109.25	
	MRCI		1.0010	1.0010		109.10	
	PES		1.0007	1.0007		109.03	
	expt ^d		1.006	1.006		109.8	

^aThe hydrogen atoms of H_2 molecule are denoted as H1 and H2, and the hydrogen atom in OH^+ is denoted as H3. ^bReference 71. ^cReference 72.^dReference 75.

in the data set $\{\vec{d}_i'\}$ is judged by $\chi(\vec{d}_i') = (\sum_{i=1}^{10} |\vec{d}_i - \vec{d}_i'|)^{1/2}$ and the new point was retained if $\chi > 0.05$ Å. All permutation equivalent points were included in such a screening. This procedure was iterated multiple times until no new points can be found. In total, 30 325 points were calculated.

In the PIP-NN fitting,^{57,58} the analytical representation the ab initio points is achieved by training feed-forward neural networks (NNs).^{59–61} The flexibility of NNs provides a high-fidelity representation of the ab initio points sampled in a large configuration space. The rigorous adaptation of the permutation symmetry in the PIP-NN method utilizes an input layer for the NN consisting of low-order PIPs, which are symmetrized monomials^{62,63}

$$G = \hat{S} \prod_{i < j}^N p_{ij}^{l_{ij}} \quad (3)$$

where N is the number of atoms in the system. $p_{ij} = \exp(-r_{ij}/a)$ are the Morse-like variables with a as an adjustable constant ($a = 2.5$ bohr was used here) and r_{ij} the $N(N-1)/2$ internuclear distances between the i th and j th atoms. l_{ij} is the degree of p_{ij} . \hat{S} is the symmetrization operator, which consists of all possible nuclear permutation operations in the system. It is worth noting that the number of PIPs in the input layer should be sufficiently large to ensure the permutation symmetry of the system.⁵⁸ For this AB_3 system, we have included all 22 low-order PIPs up to the third order. For the NN, we settled with two hidden layers with N_1 and N_2 interconnected neurons, respectively. All NN fittings were performed using the

Levenberg–Marquardt algorithm,⁶⁴ and the following root-mean-square error (RMSE) was used as the scoring function

$$\text{RMSE} = \sqrt{\sum_{i=1}^{N_{\text{data}}} (E_{\text{output}} - E_{\text{target}})^2 / N_{\text{data}}} \quad (4)$$

where E_{target} and E_{output} are the input and fitted energies, respectively. The PIP-NN method has recently demonstrated to have excellent performance in fitting PESs for several 4- and 5-atom reactive systems.^{31,58,65–67}

In each NN fitting, the data were divided randomly into three sets, namely the training (90% of the data points), validation (5%), and test (5%) sets. To avoid false extrapolation due to edge points in the randomly selected validation and test sets, only fits with similar RMSEs for all three sets were accepted. In addition, the maximum deviation is also used in selecting the final PIP-NN fits. For each architecture, 50 different training calculations were performed and the “early stopping” method was used to avoid overfitting.⁶¹ The fitting converges fast, typically finishing within a few hundred steps. The final PIP-NN PES was chosen as the average of three best fits, as suggested by the NN ensemble approach to minimize random errors.⁶⁸

The overall PES is switched from the long-range PES to the fitted PES

$$V = S V_{\text{fit}} + (1 - S) V_{\text{LR}} \quad (5)$$

where the switching function is defined

Table 2. Energies (kcal/mol) and Harmonic Frequencies (cm⁻¹) of the Stationary Points for the OH⁺ + H₂ → H₂O⁺ + H Reaction

species	method	E (kcal/mol)	frequency (cm ⁻¹)					
			1	2	3	4	5	6
OH ⁺ + H ₂	CASSCF	0	4298.1	3122.0				
	MPW1K	0	4403.2	3142.7				
	UCCSD(T)	0	4401.5	3118.7				
	MRCI	0	4399.4	3128.7				
	PES	0	4400.7	3113.6				
	expt	0	4401.2 ^a	3113.4 ^b				
(OH) ⁺ ...H ₂	CASSCF	-8.69	4051.3	2284.4	815.5	684.2	624.1	462.9
	MPW1K	-9.61	4081.7	1894.5	1145.7	795.9	741.0	711.4
	UCCSD(T)	-10.96	4139.2	1960.7	1091.4	745.2	687.7	671.2
	MRCI	-10.92	4155.2	2001.3	1055.8	729.1	678.6	660.1
	PES	-10.91	4166.0	1997.0	1040.6	730.0	670.0	665.6
	SP	-6.46	4111.5	3246.4	579.1	384.2	105.1	478.6i
(H ₂ O) ⁺ ...H	CASSCF	-25.32	3389.3	3119.4	1510.8	394.8	376.7	270.7
	MPW1K	-26.15	3353.4	2598.0	1404.4	634.9	602.0	445.7
	UCCSD(T)	-28.98	3435.3	2847.7	1459.5	544.8	541.7	384.0
	MRCI	-28.61	3435.1	2840.2	1450.7	549.2	519.3	379.5
	PES	-28.58	3434.5	2836.6	1455.6	558.1	528.9	382.1
	SP	-5.97	4172.6	3138.7	620.2	463.0	148.5	444.7i
H ₂ O ⁺ + H	CASSCF	-23.32	3346.7	3324.8	1587.9			
	MPW1K	-22.28	3442.3	3349.6	1457.2			
	UCCSD(T)	-24.09	3433.7	3376.3	1474.5			
	MRCI	-23.70	3426.7	3380.1	1495.1			
	PES	-23.66	3424.9	3386.9	1480.4			
	expt ^f	-23.8 ^c	3259.0 ^d	3212.9 ^d	1401.7 ^e			

^aReference 76. ^bReference 72. ^cReference 16. ^dReference 77. ^eReference 78. ^fVibrational frequencies.

$$S = \frac{1 - \tanh[3(\xi - 7.0)]}{2} \quad (6)$$

As a result, the PES is dominated by V_{LR} for $\xi > 7.5$ Å, while by V_{fit} $\xi < 6.5$ Å.

C. Quasi-Classical Trajectory. Standard QCT calculations for the title reaction were carried out based on the PES described above, using VENUS.^{69,70} The trajectories were initiated with a reactant separation of 10.0 Å, and terminated when products reached a separation of 7.0 Å or when reactants are separated by 9.0 Å for nonreactive trajectories. During the propagation, the gradient of the PES was obtained numerically by a central-difference algorithm. The propagation time step was selected to be 0.02 fs, which conserves the energy better than 0.04 kcal/mol for most trajectories. A few trajectories which failed to converge energy to 0.04 kcal/mol or were nonreactive after 4.0 ps were discarded. The maximal impact parameter (b_{max}) was determined using small batches of trajectories with trial values.

At each specific temperature T , the initial rovibrational energies of both OH⁺ and H₂ and relative translational energy E_{rel} between two reactants were sampled according to the Boltzmann distribution. The rate coefficient at temperature T was calculated as follows

$$k(T) = \left(\frac{8k_B T}{\pi \mu} \right)^{1/2} \pi b_{max}^2 \frac{N_r}{N_t} \quad (7)$$

where μ is the translational reduced mass, k_B is the Boltzmann constant, and N_r and N_t are the reactive and total trajectory

numbers, respectively. The standard error is given by $\Delta = [(N_t - N_r)/N_t N_r]^{1/2}$. The violation of the product zero-point energy is expected to be minimal due to the large exothermicity of the reaction.

III. RESULTS AND DISCUSSION

A. Ab Initio Characterization of Stationary Points. For the reactants (OH⁺ + H₂) and products (H₂O⁺ + H), all the ab initio methods give geometries consistent with each other, and all are in agreement with the experimental observations. As shown in Table 1, the OH⁺ and H₂ bond distances of 0.7420 and 1.0280 Å at the MRCI level compare well to the experimental values of 0.7414 and 1.0289 Å.^{71,72} But, for the relative energies and harmonic frequencies, which are listed in Table 2, only the results calculated by MRCI and UCCSD(T) are close to experimental values.¹⁶ Since no experimental data are available for the potential wells corresponding to the OH⁺...H₂ and H₂O⁺...H complexes, we have compared the results from different ab initio methods. The MRCI and UCCSD(T) results for geometries, energies, and harmonic frequencies are the closest. However, UCCSD(T) failed to yield an optimized geometry for the saddle point (SP). This failure is presumably due to the multireference character of the system, evidenced by a leading reference coefficient of 0.79 in the multistate MRCI calculations. Interestingly, the MPW1K calculation yielded an optimized SP structure, with the energy between the values of CASSCF and MRCI. On the basis of these results, the MRCI +Q scheme with the AVQZ basis set was chosen for the calculations of the PES. At this level, the geometries of reactant

and product, and the reaction energy of the title reaction are in excellent agreement with experiment.

B. Long-Range Interaction Potential in the Reactant Asymptote. Similar to the $\text{H}_2\text{O}^+ + \text{H}_2$ system,³¹ the interaction potential in the reactant asymptote for this ion–molecule reaction is dominated by electrostatic interactions, including the charge–induced dipole, charge–quadrupole, dipole–quadrupole, and dipole–induced dipole interactions. In this work, the dipole–quadrupole and dipole–induced dipole interactions were ignored, since they are shorter ranged than the charge–induced dipole and charge–quadrupole terms. Ab initio data are compared with the analytical long-range potential (V_{LR}) in Figure 2, and it is clear that the latter provides an accurate representation of the PES in this region. From the figure, it is also clear that the most favorable orientation for the charge–quadrupole interaction is $\vartheta = 90^\circ$,

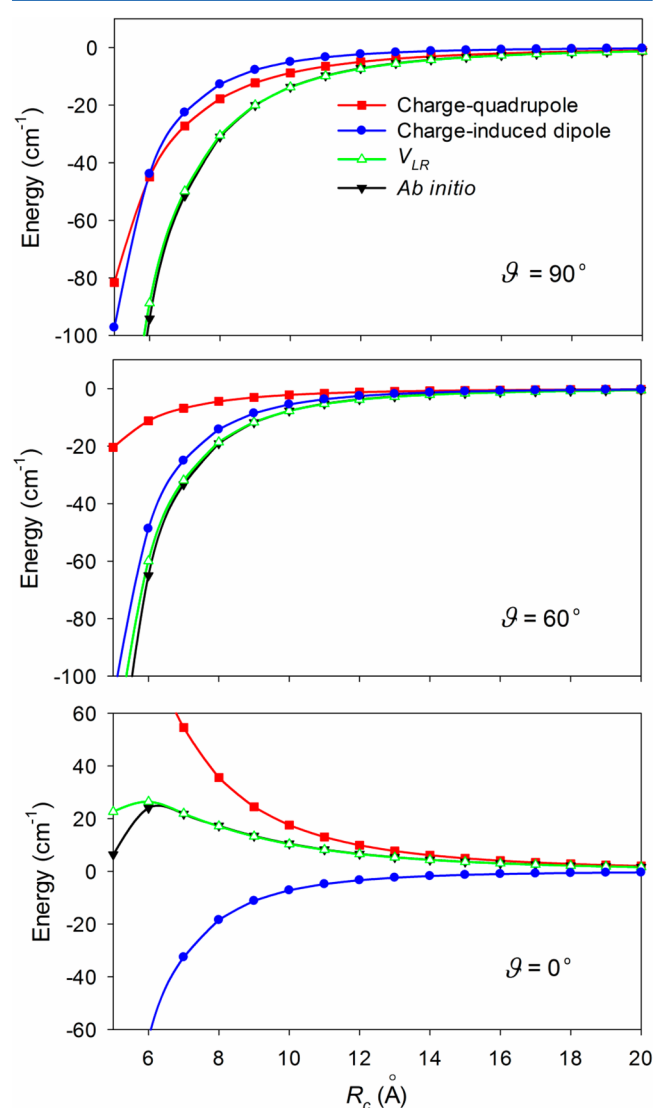


Figure 2. Comparison of ab initio energies and the long-range potential (V_{LR}) in the reactant ($\text{OH}^+ + \text{H}_2$) asymptote, in which the OH^+ and H_2 moieties are fixed at their equilibrium geometries. \bar{R}_c is the separation between the center of charge of the OH^+ ion and the center of mass of the H_2 molecule, and ϑ is the angle between \bar{R}_c and H–H internuclear bond vector.

while the charge–induced dipole interaction is most favorable at $\vartheta = 0^\circ$. As a whole, the PES is attractive and barrierless.

C. Properties of Potential Energy Surface. In the NN fitting, a two-layer NN structure, $(\text{N1} - \text{N2}) = (20 - 60)$, with 1781 parameters was employed. The RMSEs for the training/validation/test sets and maximum deviation of the three best fits are 3.7/3.8/5.4/130.1, 3.7/4.6/4.3/140.1, and 4.3/4.6/5.3/130.2 meV, respectively. The overall RMSE of the PES is 3.0 meV. From Table 1, it is clear that the PES provides a faithful representation of the MRCI stationary points. The distances are typically within 0.01 Å of the directly optimized structures, while angles are within 1° .

As shown in Figure 3, the minimum-energy path (MEP) associated with the submerged saddle point was determined on

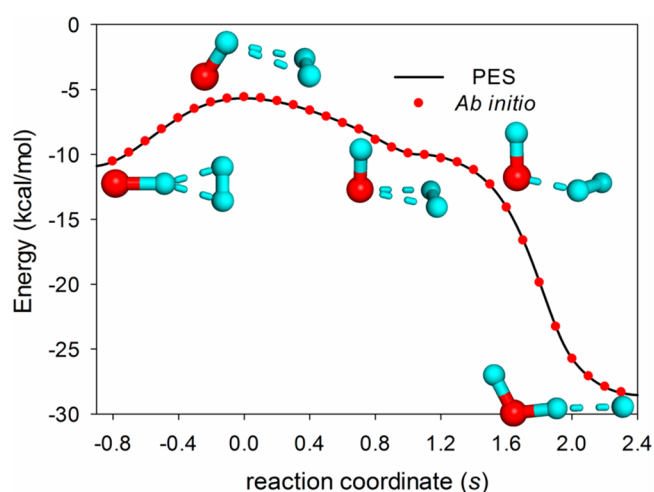


Figure 3. Minimum-energy path associated with the saddle point as a function of the reaction coordinate s . The energies are in kcal/mol and relative to the $\text{OH}^+ + \text{H}_2$ asymptote.

the fitted PES using POLYRATE 9.7,⁷³ starting from the saddle point geometry and going downhill to both (the $\text{OH}^+ \cdots \text{H}_2$ and $\text{H}_2\text{O}^+ \cdots \text{H}$) potential wells in mass-weighted Cartesian coordinates with a step size of $0.0001 \text{ amu}^{1/2} \text{ \AA}$. Along the MEP, the reaction coordinate (s) is defined as the signed distance from the saddle point ($s = 0$), with $s > 0$ referring to the product side and $s < 0$ referring to the reactant side. The MEP was followed between $s = -0.9$ and $s = 2.4 \text{ amu}^{1/2} \text{ \AA}$ and the Hessian matrix was calculated every 20 steps. Ab initio points along the MEP were subsequently calculated and the comparison with the PES is excellent, as shown in the figure. Due to the long-range electrostatic interactions discussed above, the most attractive orientation is the H_2 approaches the H end of OH^+ perpendicular to its internuclear bond vector, and all the atoms form a planar geometry of $\text{OH}^+ \cdots \text{H}_2$ complexes. However, this most attractive approach does not result directly in reaction. To react, the OH^+ first rotates to make the O end close to the H_2 molecule. The two species are nearly perpendicular after overcoming the transition state. Then, the H_2 rotates and $\text{HO}^+ - \text{H}$ bond between the O atom of OH^+ and a H atom of H_2 is partially formed.

Figure 4 displays two contour plots of the PES in the H–H distance of H_2 molecule and the center-of-mass distance R between OH^+ and H_2 while all other degrees of freedom are optimized. The main panel is in the energy range -27 to 30 kcal/mol with a large configuration space, while the inset between -24 and 30 kcal/mol shows the details around the

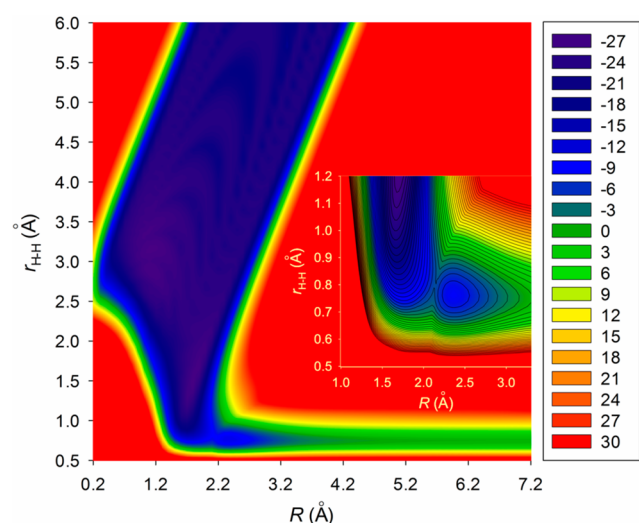


Figure 4. Contours of the fitted PES along r_{HH} and R with all other internal coordinates optimized. The main panel is from -27 to 30 kcal/mol with a contour interval of 3.0 kcal/mol, and the inset shows details around the submerged saddle point with an energy interval of 1.0 kcal/mol.

saddle point. These contour plots provide an overall perspective of the reaction pathway.

D. Kinetics. The thermal rate coefficients were computed at several temperatures, all with $b_{\text{max}} = 8.0$ Å. 50 000 trajectories were run for each temperature, with the standard errors of less than 1%. As shown in Figure 5, our calculated rate coefficients

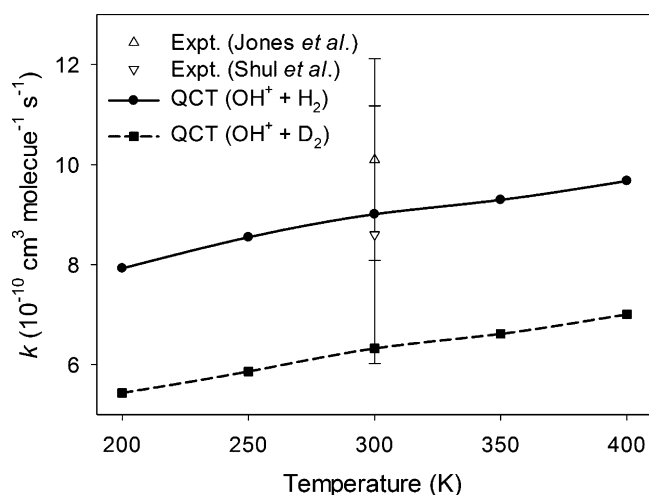


Figure 5. Temperature dependence of the calculated thermal rate coefficients for the $\text{OH}^+ + \text{H}_2$ (solid line) and $\text{OH}^+ + \text{D}_2$ (dashed line) reactions. The available experimental thermal rate coefficients^{14,16} at 300 K are also included for comparison.

are weakly dependent on temperature and in excellent good agreement with the available experimental values.^{14,16} At $T = 300$ K, the calculated rate coefficient of $9.0 \times 10^{-10} \text{ cm}^3 \text{ molecule}^{-1} \text{ s}^{-1}$ for the $\text{OH}^+ + \text{H}_2$ reaction compares well with the experimental value $(8.6 \pm 2.6) \times 10^{-10} \text{ cm}^3 \text{ molecule}^{-1} \text{ s}^{-1}$,¹⁶ and $(10.1 \pm 2.0) \times 10^{-10} \text{ cm}^3 \text{ molecule}^{-1} \text{ s}^{-1}$,¹⁴ although there is some uncertainty in the experimental data. These theory–experiment agreement validates the accuracy of the PES. In addition, the thermal rate coefficients for the $\text{OH}^+ + \text{D}_2$ reaction are also obtained from the QCT calculations, which

are smaller than those for the $\text{OH}^+ + \text{H}_2$. This kinetic isotopic effect is most likely due to the smaller zero-point energy associated with the D_2 reactant. The kinetic isotope effect is similar to that in R4 .³¹ Unfortunately, no experiment results exist for comparison.

E. Mode Specificity. The overall reaction profile along the reaction coordinate shown in Figure 3 closely resembles that for R4 . The geometry of the submerged saddle point in R3 also bears some resemblance with that for R4 . It is thus tempting to extrapolate that the two reactions might have similar kinetic and dynamical behaviors. Indeed, the calculated rate coefficient at 300 K is $9.0 \times 10^{-10} \text{ cm}^3 \text{ molecule}^{-1} \text{ s}^{-1}$ for R3 and $6.0 \times 10^{-10} \text{ cm}^3 \text{ molecule}^{-1} \text{ s}^{-1}$ for R4 .³¹ In addition, both reactions have weak temperature dependences. It is well established that R4 is significantly enhanced when the H_2O^+ rotations are excited.^{22–24} Would the rotational excitation of OH^+ also enhance the reaction?

Recently, we proposed the Sudden Vector Projection (SVP) model^{37,38} to predict mode specificity in chemical reactions. The SVP model is based on the premise that the collision between reactants happens instantly; the enhancement of reactivity by exciting a particular reactant mode is largely determined by the projection of the corresponding normal-mode vector (\vec{Q}_i) onto the reaction coordinate at the transition state (\vec{Q}_{RC}): $\eta_i = \vec{Q}_i \cdot \vec{Q}_{\text{RC}} \in [0,1]$. The SVP model has been quite successful in predicting mode specificity and bond selectivity in both gas-phase and gas–surface reactions with significant barriers.^{7,4} Although both R3 and R4 are barrierless, the submerged saddle points still provide a bottleneck for the reactions. As a result, this saddle point is expected to exert some control over the reaction and mode specificity, at least at low collision energies. Indeed, this SVP model has been successfully applied to R4 , revealing the origin of the observed rotational enhancement effect.³¹ Figure 6 illustrates the reaction

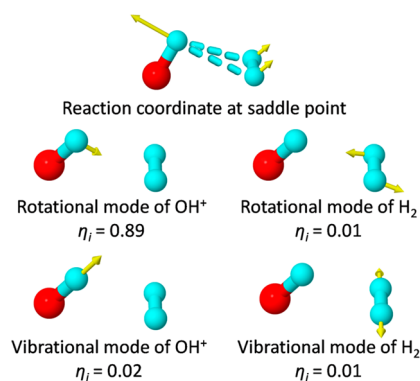


Figure 6. Depiction of the reaction coordinate vector and four reactant ro-vibrational mode vectors, along with the SVP projection values in parentheses.

coordinate vector and four reactant mode vectors (rotational and vibrational modes of OH^+ and H_2), along with the SVP projection values (η_i). It is clear that rotational mode of OH^+ has a large coupling with the reaction coordinate at the saddle point, thus suggesting a strong promotion effect for the reaction. On the other hand, neither the H_2 rotational nor the two vibrational modes has significant coupling with the reaction coordinate at this saddle point. These predictions will be tested in a future study of the reaction dynamics using both quantum and quasi-classical methods, which will lead to a more in-depth

understanding of possible mode specificity in this barrierless reaction.

IV. CONCLUSION

In this work, we report an accurate full-dimensional global PES for the title reaction based on $\sim 30\,000$ points at the MRCI+Q/AVQZ level of theory, augmented by analytical charge–quadrupole and charge–induced dipole interactions in the reactant arrangement channel asymptote. The MRCI method was used because of the significant multireference character in the system. The PES was fitted with a root-mean-square error of about 3.0 meV (24 cm^{-1}) using a recently proposed permutation invariant polynomial-neural network method, suggesting a high fidelity representation of the PES. Two potential wells ($\text{OH}^+\cdots\text{H}_2$ and $\text{H}_2\text{O}^+\cdots\text{H}$) connected by a submerged saddle point have been found on this PES.

The calculated room temperature thermal rate coefficient for the $\text{OH}^+ + \text{H}_2$ reaction is in good agreement with the available experimental data, validating the PES. A significant kinetic isotope effect has been found for the $\text{OH}^+ + \text{H}_2$ and $\text{OH}^+ + \text{D}_2$ reaction. The rate coefficients have weak temperature dependences, consistent with the barrierless reaction pathway. Using the SVP model, the reaction is predicted to be mode specific: the rotation of OH^+ is expected to significantly enhance the reaction, while the rotation of H_2 and the vibrational degrees of freedom of the two diatomic reactants are not expected to strongly influence the reactivity. We believe that the PES reported here should provide a reliable platform for future studies of the reaction dynamics of the important ion–molecular reaction.

AUTHOR INFORMATION

Corresponding Author

*E-mail: hguo@unm.edu.

Notes

The authors declare no competing financial interest.

ACKNOWLEDGMENTS

This work is supported by the Department of Energy (DE-FG02-05ER15694). The calculations were performed at the National Energy Research Scientific Computing (NERSC) Center.

REFERENCES

- (1) Herbst, E.; Klemperer, W. Formation and Depletion of Molecules in Dense Interstellar Clouds. *Astrophys. J.* **1973**, *185*, 505–533.
- (2) Watson, W. D. Interstellar Chemistry. *Acc. Chem. Res.* **1977**, *10*, 221–226.
- (3) Hollenbach, D.; Kaufman, M. J.; Neufeld, D.; Wolfire, M.; Goicoechea, J. R. The Chemistry of Interstellar OH^+ , H_2O^+ , and H_3O^+ : Inferring the Cosmic-Ray Ionization Rates from Observations of Molecular Ions. *Astrophys. J.* **2012**, *754*, 105.
- (4) Neufeld, D. A.; Goicoechea, J. R.; Sonnentrucker, P.; Black, J. H.; Pearson, J.; Yu, S.; Phillips, T. G.; Lis, D. C.; De Luca, M.; Herbst, E.; et al. Herschel/Hifi Observations of Interstellar OH^+ and H_2O^+ Towards W49n: A Probe of Diffuse Clouds with a Small Molecular Fraction. *Astron. Astrophys.* **2010**, *S21*, L10.
- (5) Gerin, M.; De Luca, M.; Black, J.; Goicoechea, J. R.; Herbst, E.; Neufeld, D. A.; Falgarone, E.; Godard, B.; Pearson, J. C.; Lis, D. C.; et al. Interstellar OH^+ , H_2O^+ and H_3O^+ Along the Sight-Line to G10.6–0.4. *Astron. Astrophys.* **2010**, *S18*, L110.
- (6) Gonzalez-Alfonso, E.; Fischer, J.; Bruderer, S.; Muller, H. S. P.; Gracia-Carpio, J.; Sturm, E.; Lutz, D.; Poglitsch, A.; Feuchtgruber, H.;

Veilleux, S.; et al. Excited OH^+ , H_2O^+ , and H_3O^+ in NGC 4418 and Arp 220. *Astron. Astrophys.* **2013**, *550*, A25.

- (7) Kubose, D. A.; Hamill, W. H. Velocity Dependence of Ion–Molecule Reaction Cross Sections in a Mass Spectrometer. *J. Am. Chem. Soc.* **1963**, *85*, 125–127.

- (8) Fehsenfeld, F. C.; Schmeltekopf, A. L.; Ferguson, E. E. Thermal-Energy Ion–Neutral Reaction Rates 7. Some Hydrogen-Atom Abstraction Reactions. *J. Chem. Phys.* **1967**, *46*, 2802–2808.

- (9) Harrison, A. G.; Thynne, J. C. J. Concurrent Ion–Molecule Reactions 4. Reactions in Mixtures of Ammonia and Water with Deuterium and Methane. *Trans. Faraday Soc.* **1968**, *64*, 945–953.

- (10) Kim, J. K.; Theard, L. P.; Huntress, W. T. ICR Studies of Some Hydrogen-Atom Abstraction Reaction: $\text{X}^+ + \text{H}_2 \rightarrow \text{XH}^+ + \text{H}$. *J. Chem. Phys.* **1975**, *62*, 45–52.

- (11) Smith, D.; Adams, N. G.; Miller, T. M. Laboratory Study of Reactions of N^+ , N_2^+ , N_3^+ , N_4^+ , O^+ , O_2^+ , and NO^+ Ions With Several Molecules at 300 K. *J. Chem. Phys.* **1978**, *69*, 308–318.

- (12) Dotan, I.; Lindinger, W.; Rowe, B.; Fahey, D. W.; Fehsenfeld, F. C.; Albritton, D. L. Rate Constants for the Reactions of H_2O^+ with NO_2 , O_2 , NO , C_2H_4 , CO , CH_4 , and H_2 Measured at Relative Kinetic Energies 0.04–2 eV. *Chem. Phys. Lett.* **1980**, *72*, 67–70.

- (13) Rakshit, A. B.; Warneck, P. A Drift Chamber Study of the Reaction $\text{ArH}^+ + \text{H}_2 \rightarrow \text{H}_3^+ + \text{Ar}$ and Related Reactions. *J. Chem. Phys.* **1981**, *74*, 2853–2859.

- (14) Jones, J. D. C.; Birkinshaw, K.; Twiddy, N. D. Rate Coefficients and Product Ion Distributions for the Reactions of OH^+ and H_2O^+ with N_2 , O_2 , NO , N_2O , Xe , CO , CO_2 , H_2S and H_2 at 300 K. *Chem. Phys. Lett.* **1981**, *77*, 484–488.

- (15) Burley, J. D.; Ervin, K. M.; Armentrout, P. B. Translational Energy Dependence of $\text{O}^+(\text{}^4\text{S}) + \text{H}_2(\text{D}_2, \text{HD}) \rightarrow \text{OH}^+(\text{OD}^+) + \text{H}(\text{D})$ from Thermal Energies to 30 eV c.m. *Int. J. Mass Spectrom. Ion Processes* **1987**, *80*, 153–175.

- (16) Shul, R. J.; Passarella, R.; Difazio, L. T.; Keesee, R. G.; Castleman, A. W. Ion Molecule Reactions Involving H_3O^+ , H_2O^+ , and OH^+ at Thermal Energy. *J. Phys. Chem.* **1988**, *92*, 4947–4951.

- (17) Sunderlin, L. S.; Armentrout, P. B. Temperature Dependence of the Reaction of O^+ with HD. *Chem. Phys. Lett.* **1990**, *167*, 188–192.

- (18) Viggiano, A. A.; Vandoren, J. M.; Morris, R. A.; Williamson, J. S.; Mundis, P. L.; Paulson, J. F.; Dateo, C. E. Rotational Temperature Dependence of the Branching Ratio for the Reaction of O^+ with HD. *J. Chem. Phys.* **1991**, *95*, 8120–8123.

- (19) Flesch, G. D.; Ng, C. Y. Absolute Total Cross-Sections for the Charge-Transfer Anddissociative Charge-Transfer Channels in the Collisions of $\text{O}^+(\text{}^4\text{S}) + \text{H}_2$. *J. Chem. Phys.* **1991**, *94*, 2372–2373.

- (20) Li, X.; Huang, Y. L.; Flesch, G. D.; Ng, C. Y. Absolute State-Selected Total Cross Sections for the Ion–Molecule Reactions $\text{O}^+(\text{}^4\text{S}, \text{}^2\text{D}, \text{}^2\text{P}) + \text{H}_2(\text{D}_2)$. *J. Chem. Phys.* **1997**, *106*, 564–571.

- (21) Flesch, G. D.; Ng, C. Y. Absolute Total Cross Sections for the Charge Transfer and Dissociative Charge Transfer Channels in the Collisions of $\text{O}^+(\text{}^4\text{S}) + \text{H}_2$. *J. Chem. Phys.* **1991**, *94*, 2372–2373.

- (22) Xu, Y.; Xiong, B.; Chang, Y. C.; Ng, C. Y. Communication: Rovibrationally Selected Absolute Total Cross Sections for the Reaction $\text{H}_2\text{O}^+(\text{X}^2\text{B}_1; v_1^+v_2^+v_3^+=000; \text{N}^+_{\text{Ka+Kc}}) + \text{D}_2$: Observation of the Rotational Enhancement Effect. *J. Chem. Phys.* **2012**, *137*, 241101.

- (23) Xu, Y.; Xiong, B.; Chang, Y. C.; Ng, C. Y. The Translational, Rotational, and Vibrational Energy Effects on the Chemical Reactivity of Water Cation $\text{H}_2\text{O}^+(\text{X}^2\text{B}_1)$ in the Collision with Deuterium Molecule D_2 . *J. Chem. Phys.* **2013**, *139*, 024203.

- (24) Li, A.; Li, Y.; Guo, H.; Lau, K.-C.; Xu, Y.; Xiong, B.; Chang, Y.-C.; Ng, C. Y. Communication: The Origin of Rotational Enhancement Effect for the Reaction of $\text{H}_2\text{O}^+ + \text{H}_2(\text{D}_2)$. *J. Chem. Phys.* **2014**, *140*, 011102.

- (25) Guo, H. Quantum Dynamics of Complex-Forming Bimolecular Reactions. *Int. Rev. Phys. Chem.* **2012**, *31*, 1–68.

- (26) Martinez, R.; Sierra, J. D.; Gonzalez, M. Cross Sections of the $\text{O}^+ + \text{H}_2 \rightarrow \text{OH}^+ + \text{H}$ Ion–Molecule Reaction and Isotopic Variants (D_2 , HD): Quasiclassical Trajectory Study and Comparison with Experiments. *J. Chem. Phys.* **2005**, *123*, 174312.

- (27) Martinez, R.; Lucas, J. M.; Gimenez, X.; Aguilar, A.; Gonzalez, M. Exact Quantum Dynamics Study of the $O^+ + H_2(v = 0, j = 0) \rightarrow OH^+ + H$ Ion–Molecule Reaction and Comparison with Quasiclassical Trajectory Calculations. *J. Chem. Phys.* **2006**, *124*, 144301.
- (28) Martinez, R.; Sierra, J. D.; Gray, S. K.; Gonzalez, M. Time Dependent Quantum Dynamics Study of the $O^+ + H_2(v = 0, j = 0) \rightarrow OH^+ + H$ Ion–Molecule Reaction and Isotopic Variants (D_2, HD). *J. Chem. Phys.* **2006**, *125*, 164305.
- (29) Xu, W. W.; Li, W. L.; Lv, S. J.; Zhai, H. S.; Duan, Z. X.; Zhang, P. Y. Coriolis Coupling Effects in $O^+(^4S) + H_2(X^1\Sigma_g^+) \rightarrow OH^+(X^3\Sigma^-) + H(^2S)$ Reaction and Its Isotopic Variants: Exact Time-Dependent Quantum Scattering Study. *J. Phys. Chem. A* **2012**, *116*, 10882–10888.
- (30) Martinez, R.; Millan, J.; Gonzalez, M. Ab Initio Analytical Potential Energy Surface and Quasiclassical Trajectory Study of the $O^+(^4S) + H_2(X^1\Sigma_g^+) \rightarrow OH^+(X^3\Sigma^-) + H(^2S)$ Reaction and Isotopic Variants. *J. Chem. Phys.* **2004**, *120*, 4705–4714.
- (31) Li, A.; Guo, H. A Nine-Dimensional Ab Initio Global Potential Energy Surface for the $H_2O^+ + H_2 \rightarrow H_3O^+ + H$ Reaction. *J. Chem. Phys.* **2014**, *140*, 224313.
- (32) Huang, X.; Carter, S.; Bowman, J. M. Ab Initio Potential Energy Surface and Vibrational Energies of H_3O^+ and Its Isotopomers. *J. Phys. Chem. B* **2002**, *106*, 8182–8188.
- (33) Huang, X.; Carter, S.; Bowman, J. Ab Initio Potential Energy Surface and Rovibrational Energies of H_3O^+ and Its Isotopomers. *J. Chem. Phys.* **2003**, *118*, 5431–5441.
- (34) Rajamäki, T.; Miani, A.; Halonen, L. Six-Dimensional Ab Initio Potential Energy Surfaces for H_3O^+ and NH_3 : Approaching the Subwave Number Accuracy for the Inversion Splittings. *J. Chem. Phys.* **2003**, *118*, 10929–10938.
- (35) Petit, A. S.; McCoy, A. B. Diffusion Monte Carlo Approaches for Evaluating Rotationally Excited States of Symmetric Top Molecules: Application to H_3O^+ and D_3O^+ . *J. Phys. Chem. A* **2009**, *113*, 12706–12714.
- (36) Petit, A. S.; Wellen, B. A.; McCoy, A. B. Unraveling Rotation-Vibration Mixing in Highly Fluxional Molecules Using Diffusion Monte Carlo: Applications to H_3^+ and H_3O^+ . *J. Chem. Phys.* **2012**, *136*, 074101.
- (37) Jiang, B.; Guo, H. Relative Efficacy of Vibrational Vs. Translational Excitation in Promoting Atom–Diatom Reactivity: Rigorous Examination of Polanyi's Rules and Proposition of Sudden Vector Projection (SVP) Model. *J. Chem. Phys.* **2013**, *138*, 234104.
- (38) Jiang, B.; Guo, H. Control of Mode/Bond Selectivity and Product Energy Disposal by the Transition State: The $X + H_2O$ ($X = H, F, O(^3P)$, and Cl) Reactions. *J. Am. Chem. Soc.* **2013**, *135*, 15251–15256.
- (39) Lynch, B. J.; Fast, P. L.; Harris, M.; Truhlar, D. G. Adiabatic Connection for Kinetics. *J. Phys. Chem. A* **2000**, *104*, 4811–4815.
- (40) Adler, T. B.; Knizia, G.; Werner, H.-J. A Simple and Efficient CCSD(T)-F12 Approximation. *J. Chem. Phys.* **2007**, *127*, 221106.
- (41) Knizia, G.; Adler, T. B.; Werner, H.-J. Simplified CCSD(T)-F12 Methods: Theory and Benchmarks. *J. Chem. Phys.* **2009**, *130*, 054104.
- (42) Feller, D.; Peterson, K. A. An Expanded Calibration Study of the Explicitly Correlated CCSD(T)-F12b Method Using Large Basis Set Standard CCSD(T) Atomization Energies. *J. Chem. Phys.* **2013**, *139*, 084110.
- (43) Knowles, P. J.; Werner, H.-J. An Efficient Method for the Evaluation of Coupling Coefficients in Configuration Interaction Calculations. *Chem. Phys. Lett.* **1988**, *145*, 514–522.
- (44) Werner, H.-J.; Knowles, P. J. An Efficient Internally Contracted Multiconfiguration–Reference Configuration Interaction Method. *J. Chem. Phys.* **1988**, *89*, 5803–5814.
- (45) Langhoff, S. R.; Davidson, E. R. Configuration Interaction Calculations on Nitrogen Molecule. *Int. J. Quantum Chem.* **1974**, *8*, 61–72.
- (46) Dunning, T. H. Gaussian Basis Sets for Use in Correlated Molecular Calculations. I. The Atoms Boron through Neon and Hydrogen. *J. Chem. Phys.* **1989**, *90*, 1007–1023.
- (47) Deskevich, M. P.; Nesbitt, D. J.; Werner, H.-J. Dynamically Weighted Multiconfiguration Self-Consistent Field: Multistate Calculations for $F + H_2O \rightarrow HF + OH$ Reaction Paths. *J. Chem. Phys.* **2004**, *120*, 7281–7289.
- (48) Dawes, R.; Jasper, A. W.; Tao, C.; Richmond, C.; Mukarakate, C.; Kable, S. H.; Reid, S. A. Theoretical and Experimental Spectroscopy of the S_2 State of CHF and CDF: Dynamically Weighted Multireference Configuration Interaction Calculations for High-Lying Electronic States. *J. Phys. Chem. Lett.* **2010**, *1*, 641–646.
- (49) Werner, H.-J.; Knowles, P. J. A Second Order Multiconfiguration SCF Procedure with Optimum Convergence. *J. Chem. Phys.* **1985**, *82*, 5053–5063.
- (50) Knowles, P. J.; Werner, H.-J. An Efficient Second-Order Mc Scf Method for Long Configuration Expansions. *Chem. Phys. Lett.* **1985**, *115*, 259–267.
- (51) Werner, H.-J.; Knowles, P. J.; Knizia, G.; Manby, F. R.; Schütz, M., et al. *Molpro, Version 2012.1*, a Package of Ab Initio Programs. See <http://www.Molpro.Net>.
- (52) Frisch, M. J.; Trucks, G. W.; Schlegel, H. B.; Scuseria, G. E.; Robb, M. A.; Cheeseman, J. R.; Scalmani, G.; Barone, V.; Mennucci, B.; Petersson, G. A., et al. *Gaussian09*; Gaussian Inc.: Wallingford, CT, 2009.
- (53) Buckingham, A. D. Permanent and Induced Molecular Moments and Long-Range Intermolecular Forces. *Adv. Chem. Phys.* **1967**, *12*, 107–142.
- (54) Simonyan, V. V.; Diep, P.; Johnson, J. K. Molecular Simulation of Hydrogen Adsorption in Charged Single-Walled Carbon Nanotubes. *J. Chem. Phys.* **1999**, *111*, 9778–9783.
- (55) Breneman, C. M.; Wiberg, K. B. Determining Atom-Centered Monopoles from Molecular Electrostatic Potentials: The Need for High Sampling Density in Formamide Conformational Analysis. *J. Comput. Chem.* **1990**, *11*, 361–373.
- (56) Li, J.; Dawes, R.; Guo, H. An Ab Initio Based Full-Dimensional Global Potential Energy Surface for $FH_2O(X^2A')$ and Dynamics for the $F + H_2O \rightarrow HF + HO$ Reaction. *J. Chem. Phys.* **2012**, *137*, 094304.
- (57) Jiang, B.; Guo, H. Permutation Invariant Polynomial Neural Network Approach to Fitting Potential Energy Surfaces. *J. Chem. Phys.* **2013**, *139*, 054112.
- (58) Li, J.; Jiang, B.; Guo, H. Permutation Invariant Polynomial Neural Network Approach to Fitting Potential Energy Surfaces. II. Four-Atomic Systems. *J. Chem. Phys.* **2013**, *139*, 204103.
- (59) Handley, C. M.; Popelier, P. L. A. Potential Energy Surfaces Fitted by Artificial Neural Networks. *J. Phys. Chem. A* **2010**, *114*, 3371–3383.
- (60) Behler, J. Neural Network Potential-Energy Surfaces in Chemistry: A Tool for Large-Scale Simulations. *Phys. Chem. Chem. Phys.* **2011**, *13*, 17930–17955.
- (61) Raff, L. M.; Komanduri, R.; Hagan, M.; Bukkapatnam, S. T. S. *Neural Networks in Chemical Reaction Dynamics*; Oxford University Press: Oxford, UK, 2012.
- (62) Xie, Z.; Bowman, J. M. Permutationally Invariant Polynomial Basis for Molecular Energy Surface Fitting Via Monomial Symmetrization. *J. Chem. Theory Comput.* **2010**, *6*, 26–34.
- (63) Braams, B. J.; Bowman, J. M. Permutationally Invariant Potential Energy Surfaces in High Dimensionality. *Int. Rev. Phys. Chem.* **2009**, *28*, 577–606.
- (64) Hagan, M. T.; Menhaj, M. B. Training Feedforward Networks with the Marquardt Algorithm. *IEEE Trans. Neural Networks* **1994**, *5*, 989–993.
- (65) Li, J.; Chen, J.; Zhang, D. H.; Guo, H. Quantum and Quasiclassical Dynamics of the $OH + CO \rightarrow H + CO_2$ Reaction on a New Permutationally Invariant Neural Network Potential Energy Surface. *J. Chem. Phys.* **2014**, *140*, 044327.
- (66) Li, J.; Guo, H. A Nine-Dimensional Global Potential Energy Surface for $NH_3(X^2A_1)$ and Kinetics Studies on the $H + NH_3 \leftrightarrow H_2 + NH_2$ Reaction. *Phys. Chem. Chem. Phys.* **2014**, *16*, 6753–6763.
- (67) Li, J.; Carter, S.; Bowman, J. M.; Dawes, R.; Xie, D.; Guo, H. High-Level, First-Principles, Full-Dimensional Quantum Calculation of the Ro-Vibrational Spectrum of the Simplest Criegee Intermediate (CH_2OO). *J. Phys. Chem. Lett.* **2014**, *5*, 2364–2369.

- (68) Zhou, Z.-H.; Wu, J.; Tang, W. Ensembling Neural Networks: Many Could Be Better Than All. *Artif. Intell.* **2002**, *137*, 239–263.
- (69) Hase, W. L.; Duchovic, R. J.; Hu, X.; Komornicki, A.; Lim, K. F.; Lu, D.-H.; Peslherbe, G. H.; Swamy, K. N.; Linde, S. R. V.; Varandas, A.; et al. Venus96: A General Chemical Dynamics Computer Program. *Quantum Chem. Prog. Exch. Bull.* **1996**, *16*, 671–679.
- (70) Hase, W. L. Classical Trajectory Simulations: Initial Conditions. In *Encyclopedia of Computational Chemistry*; Alinger, N. L., Ed.; Wiley: New York, 1998; Vol. 1, pp 399–402.
- (71) Huber, K. P.; Herzberg, G. *Molecular Spectra and Molecular Structure, IV, Constants of Diatomic Molecules*; van Norstrand: Princeton, NJ, 1979.
- (72) Merer, A. J.; Malm, D. N.; Martin, R. W.; Horani, M.; Rostas, J. Ultraviolet Emission-Spectra of OH^+ and OD^+ - Rotational Structure and Perturbations in $\text{A}^3\Pi - \text{X}^3\Sigma^-$ Transition. *Can. J. Phys.* **1975**, *53*, 251–283.
- (73) Corchado, J. C.; Chuang, Y.-Y.; Fast, P. L.; Hu, W.-P.; Liu, Y.-P.; Lynch, G. C.; Nguyen, K. A.; Jackels, C. F.; Fernandez Ramos, A.; Ellingson, B. A., et al. *Polyrate, Version 9.7*; University of Minnesota: Minneapolis, MN, 2007.
- (74) Guo, H.; Jiang, B. The Sudden Vector Projection Model: Mode Specificity and Bond Selectivity Made Easy. *Acc. Chem. Res.* **2014**, DOI: 10.1021/ar500350f.
- (75) Strahan, S. E.; Mueller, R. P.; Saykally, R. J. Measurement of the Rotational Spectrum of the Water Cation (H_2O^+) by Laser Magnetic Resonance. *J. Chem. Phys.* **1986**, *85*, 1252–1260.
- (76) Irikura, K. K. Experimental Vibrational Zero-Point Energies: Diatomic Molecules. *J. Phys. Chem. Ref. Data* **2007**, *36*, 389–397.
- (77) Huet, T. R.; Pursell, C. J.; Ho, W. C.; Dinelli, B. M.; Oka, T. Infrared Spectroscopy and Equilibrium Structure of $\text{H}_2\text{O}^+(\text{X}^2\text{B}_1)$. *J. Chem. Phys.* **1992**, *97*, 5977–5987.
- (78) Forney, D.; Jacox, M. E.; Thompson, W. E. The Vibrational Spectra of Molecular Ions Isolated in Solid Neon. X. H_2O^+ , HDO^+ , and D_2O^+ . *J. Chem. Phys.* **1993**, *98*, 841–849.